The role of transition radiation in cathodoluminescence imaging and spectroscopy of thin-foils

BG Mendis[1], A Howkins[2], D Stowe[3], JD Major[4] and K Durose[4]

1. *Dept. of Physics, Durham University, South Road, Durham, DH1 3LE, UK*
2. *Experimental Techniques Centre, Brunel University, Uxbridge, UB8 3PH, UK*
3. *Gatan UK, 25 Nuffield Way, Abingdon, Oxfordshire, OX14 1RL, UK*
4. *Stephenson Institute for Renewable Energy, University of Liverpool, Liverpool, L69 7ZF, UK*

Abstract

There is renewed interest in cathodoluminescence (CL) in the transmission electron microscope, since it can be combined with low energy loss spectroscopy measurements and can also be used to probe defects, such as grain boundaries and dislocations, at high spatial resolution. Transition radiation (TR), which is emitted when the incident electron crosses the vacuum-specimen interface, is however an important artefact that has received very little attention. The importance of TR is demonstrated on a wedge shaped CdTe specimen of varying thickness. For small specimen thicknesses (<250 nm) grain boundaries are not visible in the panchromatic CL image. Grain boundary contrast is produced by electron-hole recombination within the foil, and a large fraction of that light is lost to multiple-beam interference, so that thicker specimens are required before the grain boundary signal is above the TR background. This is undesirable for high spatial resolution. Furthermore, the CL spectrum contains additional features due to TR which are not part of the 'bulk' specimen. Strategies to minimise the effects of TR are also discussed.

1.0 Introduction

Cathodoluminescence (CL) in the electron microscope is a powerful technique for probing radiative transitions in dielectrics [1], plasmons [2-3], defect properties [4-6], strain [7] and carrier lifetime [8-10] at high spatial resolution. CL is typically implemented in a scanning electron microscope (SEM), but recently there has been renewed interest in its application as a transmission electron microscope (TEM) technique. There are several reasons for this. The first is that CL can be combined with electron energy loss spectroscopy (EELS) in the TEM, which measures both radiative and non-radiative energy loss events and is therefore complementary to CL [2]. Advances in monochromation have also enabled the detection of the EELS signal at deep infra-red wavelengths [11-12]. The second reason is that for incoherent luminescence (i.e. light emitted by electron-hole pair recombination) the spatial resolution of TEM-CL is superior to SEM-CL. This is due to reduced elastic scattering of the high energy electron beam within a thin-foil compared to a bulk specimen. The higher spatial resolution is ideal for analysis of nano-structures (e.g. quantum wells) as well as atomic-scale defects (e.g. dislocations, grain boundaries).

Here we have imaged grain boundaries in CdTe using CL in both the SEM and TEM. The initial motivation was to examine the role of surface recombination on CL imaging,

especially for TEM-CL, where the effect should be larger due to the thin-foil geometry. It was observed that the grain boundary contrast in TEM-CL was anomalously low, despite Monte Carlo simulations and SEM-CL results predicting otherwise. The discrepancy was shown to be due to transition radiation, i.e. the light emitted when the high energy electron enters and exits the thin-foil [13-14]. The incoherent luminescence, which is the useful signal for grain boundary imaging, is therefore superimposed on a coherent luminescence background due to transition radiation. If the latter is sufficiently large the overall CL image contrast is reduced and the CL spectrum contains additional features. This is similar to the well-known 'Stobbs' factor in TEM phase contrast imaging [15] and 'spurious' Cerenkov losses in EELS spectra [16-17]. Transition radiation from thin foils has been reported previously [18-21], but to our knowledge this is the first demonstration of its importance in high spatial resolution CL imaging and spectroscopy. The results highlight the importance of transition radiation in interpretation of TEM-CL data.

The paper is organised as follows. In the next section (section 2) experimental details and computational methods are presented. The latter consist of Monte Carlo methods to simulate the steady state carrier distribution volume for incoherent luminescence as well as calculation of the coherent transition radiation. SEM-CL and TEM-CL experimental data are presented in section 3 along with simulation results to aid the discussion. SEM-CL is a key part to ruling out surface recombination as the source of the anomalous grain boundary contrast in TEM-CL as well as characterising the emission characteristics of the material. In section 4 the implications of transition radiation for TEM-CL analysis are discussed along with strategies to minimise its effect. Finally conclusions are presented in section 5.

2.0 Experimental and computational details

2.1 *Experimental Methodology*

The sample investigated is a ~2.5 μm thick polycrystalline CdTe layer deposited by close space sublimation [22]. CdTe is an exemplar thin-film photovoltaic material and there is considerable interest in its grain boundary optoelectronic properties. The device consists of the following sequence of layers: glass superstrate, fluorine doped SnO_2, ZnO, CdS and CdTe. There is some inter-diffusion of sulphur from CdS into the CdTe, although the sulphur concentration rapidly decreases to ~5 at% within ~100 nm of the interface [22]. Furthermore, the sample has undergone a $CdCl_2$ activation treatment to improve the device efficiency [22]. The CdTe is effectively chlorine doped during this process. Flat samples for SEM-CL were prepared by Ar broad ion-beam polishing a small section (2x1 mm) of the device at 1 keV ion energy and 2° incident angle. The sample was examined at room temperature in plan-view using a Hitachi SU70 FEG SEM equipped with a Gatan MonoCL system. A photomultiplier tube was used for panchromatic CL imaging. The dark signal was determined by blanking the beam and was subtracted from the panchromatic CL images. A Faraday cup was used to measure the beam current.

A TEM wedge shape sample (wedge angle 2.5°) was prepared using an FEI Helios 600 focussed ion-beam (FIB) microscope. A wedge geometry allows examination of a range of thicknesses within the same specimen. Final thinning of the specimen was done at 5 keV ion-

beam energy to minimise Ga-beam damage. The thickness along the specimen wedge was measured using EELS in the Durham JEOL 2100F FEG TEM operating at 200 kV. Convergent beam electron diffraction (CBED) was used to measure the absolute specimen thickness at a reference point [23] and thereby calibrate the EELS inelastic mean free path. The gradient in the EELS thickness profile was consistent with a 2.5° wedge angle.

The specimen was examined at room temperature in the Brunel JEOL 2100F FEG TEM operating at 80 kV. The microscope is equipped with a Gatan Vulcan CL system, which has two ellipsoidal mirrors positioned above and below the specimen, giving 57% collection efficiency (i.e. 7.2 steradian solid angle). The high angle annular dark field (HAADF) signal was acquired simultaneously with the CL signal in scanning TEM (STEM) mode. For incoherent imaging conditions (i.e. large detector inner angle) and non-channeling specimen orientations the HAADF signal is proportional to the specimen thickness [24]. In order to approximate these conditions the camera length was adjusted so that the HAADF detector inner angle was nearly six times as large as the STEM probe semi-convergence angle. The CL signal was evaluated as a function of the HAADF intensity, which is an indirect measure of the specimen thickness. A photomultiplier tube, operated in pulse counting mode, and CCD camera was used for acquiring CL panchromatic images and spectrum images respectively.

2.2 *Computational details*

The Monte Carlo method [25] was used to simulate the excess minority carrier distribution volume due to the electron beam. Radiative recombination of electron-hole pairs within this volume gives rise to the incoherent luminescence that produces grain boundary contrast in CL images. The first stage of the simulation involves calculating the electron-hole pair generation function of the incident electron beam. A screened Rutherford cross-section was used for elastic scattering, while inelastic scattering was modelled using a modified Bethe stopping power that is also valid for small electron energies [25]. The *average* electron-hole pair energy for CdTe was 4.65 eV [26] and carrier generation was assumed to take place uniformly along the trajectory segment of the incident electron. Trajectories from 10^5 electrons incident normal to the specimen surface were simulated in two dimensions for statistically significant results. The convergence angle and diameter of the probe were not taken into account, since these have only a secondary effect on the carrier distribution volume, which is governed primarily by the minority carrier diffusion length in CdTe (see below).

From the simulated electron-hole pair generation function (g) the time evolution of the carriers (n) was modelled via the continuity equation [27]:

$$\frac{\partial n(\mathbf{r},t)}{\partial t} = D\nabla^2 n(\mathbf{r},t) + g(\mathbf{r}) - \frac{n(\mathbf{r},t)}{\tau} \quad \text{... (1)}$$

where ∇^2 is the Laplacian. The dependence of the terms on the spatial coordinate vector $\mathbf{r}$ and time t is indicated. The minority (i.e. electron) carrier lifetime (τ) was assumed to be 1 ns

[28], while a value of 8.28 cm^2/s was used for D [29]. The latter is based on electrical measurements of CdTe thin-film photovoltaic devices [29]. For these conditions the carrier diffusion length ($L = (D\tau)^{½}$) is 910 nm. In our measurements the CL acquisition time per pixel was many micro-seconds, i.e. considerably longer than the lifetime, so that steady-state conditions were established and $\partial n/\partial t = 0$. Steady-state was numerically approximated by calculating the time evolution of carriers (via Eq. 1 using finite difference methods) for a total time of three lifetimes.

Free surfaces in the specimen impose boundary conditions which must be satisfied at all times, i.e.:

$$S_{\mathrm{sur}} n_{\mathrm{sur}} = \left| D \frac{\partial n}{\partial z} \right|_{z=0} \qquad \ldots (2)$$

n_{sur} is the carrier concentration at the surface and z is the spatial coordinate along the surface normal (the surface is at $z = 0$). S_{sur} is the surface recombination velocity. The left hand side of Eq. (2) is the surface recombination rate [27], while the right hand side is the carrier flux diffusing towards the surface to replenish carriers lost to recombination. For a TEM thin-foil Eq. (2) must be applied to both the beam entrance and exit surfaces. A value of 10^5 cm/s was used for the surface recombination velocity [27]. Some simulations also included a grain boundary; the boundary condition at the grain boundary is physically equivalent to a free surface, apart from the fact that carriers can now diffuse from the two neighbouring grains towards the grain boundary (cf. Eq. (2)). The ratio of grain boundary to surface recombination velocity was assumed to be 0.5, 0.25 or 0.1 (see section 3.1).

The incoherent luminescence intensity is taken to be directly proportional to the number of steady state carriers. The constant of proportionality includes the radiative recombination efficiency, i.e. the probability that an electron-hole pair will decay radiatively. Compared to a perfect crystal the radiative recombination efficiency will typically be lower in the vicinity of a grain boundary and/or free surface. Strictly speaking therefore it is not possible to directly compare the incoherent luminescence intensity for crystals with and without a grain boundary via the number of steady state carriers alone. This will have some effect on the absolute grain boundary contrast values reported in section 3, although we do not expect it to fundamentally alter the conclusions derived from the simulation results.

While Monte Carlo simulations are used to estimate the incoherent luminescence, calculating the coherent transition radiation is more straightforward. The double differential cross-section for the number of photons (N) emitted due to a single electron incident in a foil of thickness $2a$ and complex dielectric constant ε is given by [14]:

$$\frac{\partial^2 N}{\partial E \partial \Omega} = \frac{2e^2}{\pi \hbar c E} \left| \frac{\varepsilon - 1}{1 + (\sin^2\theta - \varepsilon)\beta^2} \right|^2 \cdot \frac{\beta^6 \cos^2\theta}{(1 - \beta^2 \cos^2\theta)^2} \cdot \left| P^+ + f P^- \right|^2 \qquad \ldots (3)$$

where E is the photon energy, Ω the solid angle for polar angle θ, while e, h and c are physical constants for the electronic charge, Planck's constant and speed of light respectively. β is the speed of the incident electron divided by the speed of light and f is equal to +1 (-1) for transition radiation emitted at the beam exit (entrance) side of the foil . The other parameters are:

$$P^{\pm} = \frac{\sin\theta\left[\beta\bar{\lambda}\left\{\begin{matrix}\tanh(\bar{\lambda}\bar{a})\cos K\\ -i\coth(\bar{\lambda}\bar{a})\sin K\end{matrix}\right\}-\left(\frac{1}{\beta^2}+\sin^2\theta-\varepsilon-1\right)\left\{\begin{matrix}\sin K\\ i\cos K\end{matrix}\right\}\right]}{i\varepsilon|\cos\theta|+\bar{\lambda}\left\{\begin{matrix}\tanh(\bar{\lambda}\bar{a})\\ \coth(\bar{\lambda}\bar{a})\end{matrix}\right\}}$$

$$\bar{\lambda}=\sqrt{\sin^2\theta-\varepsilon}\ ;\ \ \bar{a}=2\pi aE/hc\ ;\ K=\bar{a}/\beta \qquad \ldots (4)$$

The upper and lower terms in the curly brackets are valid for P^+ and P^- respectively [14]. Eqs. (3) and (4) are only applicable for normal electron beam incidence; the general case of oblique incidence is given in [14]. Numerically integrating Eq. (3) over all solid angles gives the transition radiation spectrum. The complex dielectric constant for CdTe reported in [30] was used in the calculation. Eq. (3) potentially includes any Cerenkov radiation escaping the specimen, although for normal beam incidence and flat specimens this contribution is negligible in CdTe due to total internal reflection at the foil surfaces [14, 20].

3.0 Results and Discussion

3.1 *SEM-CL results*

SEM-CL was used to determine the emission characteristics of grain interior and grain boundary regions in CdTe, as well as analyse the role of surface recombination on grain boundary contrast. Figure 1a is a panchromatic CL image of polycrystalline CdTe acquired at 15 keV electron beam energy. Panchromatic CL images of the same region were also acquired at 5 and 10 keV, while varying the current at a given beam energy. The CL intensity as a function of electron beam power can then be plotted for the grain interiors (e.g. 'G1', 'G2' and 'G3' in Fig. 1a), as well as grain boundaries (e.g. 'GB1', 'GB2' and 'GB3' in Fig. 1a). The approximate regions from which the CL intensity was extracted are shown in Fig. 1a. For grain boundaries the CL intensity was extracted from a region ~670 nm wide (i.e. five image pixels), as measured along the boundary plane normal. Figures 1b and 1c plot the CL intensity vs electron beam power for the grain interior G1 and grain boundary GB1. The data points are fitted to a curve of the form $A(P\text{-}P_o)^k$, where A, P_o and k are constants and P is the power. An initial estimate was made for P_o and the logarithm of the CL intensity was plotted as a function of $\log(P\text{-}P_o)$. This gives a straight line, with intercept $\log(A)$ and gradient k. Best estimates for A, P_o and k were taken as those values that minimised the regression coefficient of the straight line. Table 1 summarises the results for the different regions labelled in Fig. 1a.

The power dependence of the CL intensity for different recombination mechanisms has been investigated theoretically by Schmidt *et al* [31]. At steady state the k-exponent has values

between 1 and 2 for excitonic emission, while $k < 1$ for impurity related transitions, such as free to bound and donor acceptor pair recombination [31]. The *k*-values for grain interiors is similar to grain boundaries (Table 1) and is ~1.4, which suggests that the dominant recombination mechanism is exciton-related. The results are consistent with room temperature photoluminescence measurements on *p*-type CdTe [32]. This is however not to be confused with the well-known behaviour of CdTe at low temperature (i.e. liquid nitrogen/helium cooled), where enhanced donor acceptor pair recombination is observed at the grain boundaries [10, 33-34]. P_o is the power lost to backscattered electrons and non-radiative recombination at a free surface and/or grain boundary. It should be higher for a probe incident along a grain boundary, since then non-radiative recombination takes place at both the surface and grain boundary, compared to only surface recombination for a probe incident within the grain interior. The data is however not sufficiently accurate to reproduce this trend in Table 1. This suggests that for our sample the surface recombination velocity is significantly higher than that due to the grain boundary.

Figures 2a, 2b and 2c are panchromatic CL images of the same CdTe region acquired at 15, 10 and 5 keV, with an almost constant power of 20 µW. The CL intensity profiles across the central grain boundary (arrowed in Fig. 2a) for each beam energy are shown superimposed in Figure 2d. The average 'plateau' intensities within the grain interiors 'G1' and 'G2' (Fig. 2a) have been normalised to 100% for a direct comparison. The average half-width of the grain boundary profiles decrease monotonically with beam energy and has values of 1.2 µm at 15 keV, 0.6 µm at 10 keV and 0.5 µm at 5keV. The grain boundary contrast is calculated using the formula $[1-(I_{min}/I_o)]$, where I_{min} is the minimum intensity at the grain boundary and I_o is the average 'plateau' intensity within the two neighbouring grain interiors. The contrast values extracted from Fig. 2d are 58% for 15 keV, 60% for 10 keV and 48% for 5 keV respectively. Unlike the profile width there is no obvious trend in grain boundary contrast. For a given grain boundary the contrast is dependent on two parameters. The first is the size of the steady state carrier distribution volume. Lower beam energies have smaller carrier volumes, so that the minority carriers have a shorter distance to diffuse towards the grain boundary and undergo recombination. This increases the grain boundary contrast. On the other hand surface recombination should lower grain boundary contrast, especially if the recombination velocity for the surface is much larger than the grain boundary, a fact established for our sample from the P_o values in Table 1. Fig. 5d highlights the opposing effects of surface recombination and carrier volume size on grain boundary contrast. Apart from the lowest beam energy of 5 keV the effect of surface recombination appears to be partly or wholly mitigated by the carrier volume size.

Monte Carlo simulations can also be used to predict grain boundary contrast. The total number of carriers at steady state (N_{eh}) is calculated for the two cases of a crystal with and without a grain boundary. For the former the electron beam is incident along the grain boundary which is oriented end-on to the specimen surface. The simulated grain boundary recombination velocity was either 0.5, 0.25 or 0.1 the value of the surface recombination velocity (i.e. 10^5 cm/s). These values were selected based on the CL intensity vs power results (Table 1), which indicated a relatively low recombination velocity for the grain boundary compared to the free surface. Figure 3 shows exemplar steady state carrier distribution volumes at 5 and 15 keV for a crystal with and without a grain boundary. The

incoherent luminescence intensity was taken to be proportional to N_{eh}^{k}, where k = 1.4 based on the average values for grain interiors and grain boundaries listed in Table 1. The grain boundary contrast was calculated using the formula $[1-(N_{eh}^{k})_{gb}/(N_{eh}^{k})_{bulk}]$, where the subscripts 'gb' and 'bulk' refer to the N_{eh}^{k} values for the crystal with and without a grain boundary respectively. The grain boundary contrast for the different simulation parameters is summarised in Table 2. A small (~10%) increase in contrast is predicted as the beam energy is decreased from 15 to 5 keV. This is not fully consistent with experiment, although it is perhaps not surprising given the uncertainly in many parameters (e.g. surface/grain boundary recombination velocity, carrier diffusion length etc). Note also that the simulated contrast values are much smaller than experiment. However, Table 2 does confirm the importance of the size of the carrier distribution volume even in the presence of strong surface recombination.

3.2 *TEM-CL results*

Figure 4 is a many beam, bright-field TEM image of the wedge sample acquired at 200 kV, with the different layers annotated. There is a gradual darkening of the specimen along the length direction due to the wedge geometry. The CdTe layer contains a number of grain boundaries throughout the wedge. Figures 5a and 5b show HAADF and panchromatic CL images of the sample acquired simultaneously at 80 kV. The integrated HAADF and CL intensities for the CdTe layer as a function of position along the sample wedge (i.e. length direction) were extracted from the box region in Fig. 5a and are shown superimposed in Figure 5c. The small pores at the CdS-CdTe interface (Figs. 4 and 5a) were used as reference points to correlate Fig. 5c with the EELS thickness profile, which was measured in a separate microscope. The specimen thickness at a given position along the wedge region could therefore be estimated. There was however some damage to the thinnest regions of the specimen when transferring between microscopes, so that the smallest measured thickness using EELS was 185 nm (this position is marked by an arrow in Fig. 5c). The HAADF intensity varies linearly between positions of ~1-3 μm along the wedge, as expected for a uniform wedge shape. FIB milling is likely to be imprecise at the specimen edge, which would give rise to a non-ideal shape and therefore the non-linear HAADF intensity profile for positions <1 μm. On the other hand the plateauing of HAADF intensity for positions >3 μm is likely to be an artefact due to residual diffraction contrast between grains. Indeed the EELS thickness profile which was acquired at 200 kV, where there is less scattering, showed a linear trend in this region, indicating a wedge geometry.

The CL and HAADF profiles have a similar shape for thicknesses > 94 nm (i.e. beyond ~1.2 μm position; Fig. 5c). This thickness was estimated by taking into account the 2.5° wedge angle and measured EELS thickness of 185 nm at ~3.3 μm position. For smaller thicknesses the CL intensity increases dramatically, as evident from the features labelled 'edge emission' in Fig. 5c. The intensity increase is observed not just for CdTe, but for the SnO_2, ZnO and Pt layers as well (Fig. 5b), which suggests that the effect is not related to the dielectric constant of the material. Multiple beam interference calculations indicate that the light escaping a parallel sided foil can be as low as ~11 or 24% depending on polarisation (see Appendix). At the specimen edge however the sample no longer consists of parallel surfaces, so that the contribution from total internal reflection and interference of the light is modified, which

could explain the higher CL intensity. There is also a higher CL intensity at 260 nm specimen thickness (Fig. 5c), which is noticeable in the panchromatic CL image (see arrow in Fig. 5b). This could also be due to multiple beam interference, since a higher intensity is predicted at ~290-300 nm thickness, although the theoretical increase is larger than experiment (see Appendix for more details).

Grain boundaries are only visible in the panchromatic CL image for thicknesses >250 nm, although they are present in the thinner regions as well (Fig. 4). CL intensity profiles across two grain boundaries, labelled 'GB1' and 'GB2', are extracted from the box regions in Fig. 5b and are shown superimposed in Figure 5d. The profiles have an average half-width of 170 and 190 nm respectively and low contrast values of 18 and 23%. Several factors may contribute to the reduced visibility of grain boundaries in the thinner regions, such as grain boundary projected width, misorientation as well as reduced signal to noise ratio of the CL intensity. Grain boundaries that are inclined to the incident beam should have lower contrast compared to those that are 'end-on'. However, the CL intensity profile is significantly broadened by the large carrier diffusion length in CdTe; for example the measured half-width in Fig. 5d is greater than 150 nm. The grain boundaries in Fig. 4 however do not have comparable projected width. Highly misoriented 'regular' grain boundaries would also have higher CL contrast compared to say coincident site lattices (e.g. twin boundaries). There is however evidence of 'regular' grain boundaries present throughout the specimen, as can be seen from the abrupt change in diffraction contrast between neighbouring grains in Fig. 4. Hence grain boundary projected width and misorientation are unlikely to be the cause of the reduced contrast. Finally consider signal to noise ratio. The minimum contrast detected is approximately the reciprocal of the signal to noise ratio. Poisson statistics is used to determine the signal to noise in different regions of the specimen using the CL intensity profile in Fig. 5c. Thus the minimum detected contrast varies between 8-10% for specimen thicknesses between ~94 nm and ~250 nm (see Fig. 5c). The grain boundaries in Fig. 5d however have twice as much contrast, so that signal to noise ratio can also be ruled out. Note that this includes the role of any surface damage layers from FIB milling, which are likely to be non-radiative and have a larger volume fraction for thinner regions of the specimen.

Monte Carlo simulated carrier distribution volumes at steady state are shown in Figure 6 for 50 and 250 nm thick foils with and without a grain boundary. Table 3 summarises the grain boundary contrast values predicted by Monte Carlo simulations for specimens of varying thickness. The contrast was calculated using the procedure described in section 3.1. For a given grain boundary the contrast increases monotonically with decreasing foil thickness, which suggests that the smaller carrier volume in thin-foils has a larger effect than surface recombination. Furthermore, grain boundary contrast is predicted to be stronger in TEM-CL compared to SEM-CL (Tables 2 and 3). However, these trends are not consistent with the panchromatic CL image of Fig. 5b, where the contrast of grain boundaries in the thinnest regions of the foil is below the signal to noise level.

Figure 7a shows the CL spectrum extracted from ~280 nm thick CdTe, i.e. close to the grain boundaries 'GB1' and 'GB2' in Fig. 5b. The room temperature SEM-CL [10] and photoluminescence [32] spectrum for CdTe consists of a peak at ~820 nm wavelength as well as a high energy tail extending to ~760 nm wavelength. This is evident in Fig. 7a, although

there is a further broad peak centred around 600 nm. The contribution from this extra intensity is significant; indeed only ~31% of the total intensity lies within the expected wavelength range for CdTe (i.e. 760-850 nm). Figure 7b shows the transition radiation spectrum for 280 nm thick CdTe calculated using Eqs. (3) and (4). Wavelengths beyond 850 nm were not calculated, since the CdTe dielectric constants reported in [30] did not cover this range. There is a broad peak centred at ~526 nm, which could explain the extra intensity in Fig. 7a, although finer details of the experimental and theoretical peak shapes do not match. The discrepancy can be due to several factors. For example the calculation assumes a parallel sided foil, while in reality the specimen is wedge shaped. In fact changing the thickness by only ±20 nm in the calculation causes a peak shift. This is illustrated in Fig. 7b where the transition radiation spectra for 260 and 300 nm thick foils have been superimposed. The presence of an oxide or contamination layer on the specimen surface can also have an effect [13,14].

As further proof that the broad peak at 600 nm wavelength is due to transition radiation a spectrum image was acquired across the CdTe region containing the grain boundaries 'GB1 and 'GB2' (Fig. 5b). Figure 7c shows the integrated intensity map for wavelengths in the 760-850 nm range, which spans the CdTe 'bulk' spectrum. Grain boundaries are clearly resolved and the contrast values for GB1 and GB2 are 38% and 53% respectively, which is similar to the Mont-Carlo simulations. Grain boundaries are however not observed when the integration window is shifted to the 400-700 nm wavelength range (Figure 7d), which corresponds to the broad feature at 600 nm. Instead a constant intensity is observed within the CdTe layer, consistent with transition radiation generated at the specimen surfaces. Note that the slight increase in intensity near the CdS-CdTe interface is likely to be due to sulphur diffusion [22], since CdS_xTe_{1-x} is known to have different dielectric properties to CdTe [30]. In fact the CL spectrum acquired from near the CdS-CdTe interface showed a blue shift of the 600 nm broad peak to ~534 nm wavelength. Furthermore, the 820 nm peak associated with the CdTe 'bulk' specimen had red shifted to ~838 nm wavelength due to band gap narrowing in CdS_xTe_{1-x} [22, 30]. Interestingly the enhanced CL emission at ~260 nm thickness, which is thought to be due to multiple beam interference of the incoherent luminescence generated from within the specimen, is also absent in Fig. 7d, but not Fig. 7c, as required.

Figure 8a plots the number of transition radiation photons for a single incident electron at 80 kV as a function of specimen thickness. The number of photons was calculated by integrating the transition radiation spectrum over the 350-850 nm wavelength range. The shape of the curve is surprisingly similar to the CL intensity profile in Fig. 5c for specimen thicknesses >100 nm, i.e. there is a linear increase followed by a 'plateauing' of the number of photons for thicknesses >200 nm. In Figure 8b the number of Monte Carlo simulated carriers at steady state is plotted as a function of specimen thickness. The number of carriers increases monotonically with foil thickness for the range examined (up to 300 nm).

The anomalous low grain boundary contrast in panchromatic TEM-CL can now be explained as follows: incoherent luminescence is generated within the foil and gives rise to any grain boundary contrast in the CL image. For the majority of foil thicknesses a significant fraction of the light is lost to total internal reflection and destructive interference (see Appendix).

Coherent transition radiation on the other hand is generated at the interface between two dielectric media, i.e. when the electron beam enters or exits the specimen. Figures 8c and 8d are polar diagrams of the angular distribution of the transition radiation at 600 and 820 nm wavelengths emitted from a 280 nm thick foil. The radiation emitted along the foil normal or at glancing angle to the specimen is negligible. This means that the transition radiation is readily collected by the ellipsoidal mirrors located above and below the TEM specimen. The light detected for small specimen thicknesses will therefore be dominated by transition radiation, so that the overall grain boundary contrast is lower. For CdTe thicknesses >200 nm however the transition radiation 'saturates', while the incoherent luminescence signal continues to increase (Figs. 8a and 8b). Grain boundaries eventually become visible in the CL image, although with reduced contrast. Furthermore, the CL spectrum also contains a significant contribution from the transition radiation (Fig. 7a).

4.0 Implications for TEM-CL measurements

From the previous section it is clear that transition radiation is an important 'artefact' that complicates interpretation of TEM-CL data. In the example reported here foil thicknesses >250 nm are required before the incoherent luminescence contribution becomes apparent. The relatively large specimen thickness is undesirable for investigating defects such as grain boundaries and dislocations at high spatial resolution. One way to overcome this is to cryogenically cool the sample, so that the radiative recombination efficiency is higher and there is more light generated for a given number of carriers. The minimum specimen thickness for observing the incoherent luminescence is therefore reduced. Boyall *et al* [35] developed an incoherent luminescence model to describe the thickness dependence of the panchromatic TEM-CL intensity for GaN at 100 K, the role of transition radiation being presumably small when the radiative recombination efficiency of the specimen is large. However, a potential drawback to specimen cooling is that the recombination mechanisms at low temperature may be different to room temperature and might therefore not be a viable option. As an alternative lower incident electron beam energies reduce the transition radiation [18] and also generate more carriers within a given foil thickness. Both these effects are desirable, but it is not clear whether the lower spatial resolution at low beam energies is a deciding factor. More work needs to be done to investigate this aspect further.

A more straightforward way of minimising transition radiation is apparent from the polar diagrams in Figs. 8c and 8d. The emission pattern is asymmetric, with more radiation being emitted from the beam exit side of the specimen. Incoherent luminescence on the other hand is isotropic. This means that instead of collecting light from two CL ellipsoidal mirrors, the light from only the mirror on the side of least transition radiation should be collected. The appropriate mirror depends on the dielectric constant and thickness of the specimen. For a 280 nm thick CdTe specimen it is the mirror on the beam entrance side, but for a 50 nm thick CdTe specimen the asymmetry is reversed and hence the opposite mirror must be used. A simple test to determine the appropriate mirror is to examine the CL spectrum acquired separately from the top and bottom mirror, focussing on the wavelengths that are not part of the 'bulk' spectrum. Monochromation of the CL image is also beneficial if the transition radiation is strongest at wavelengths different from those of interest. For example in the present case this would mean filtering out the broad peak at 600 nm (Fig. 7). If angle resolved

CL can be performed by imaging the light collected from a mirror using a 2D CCD camera then the coherent and incoherent contributions can be further separated as described in [36] for SEM-CL. Angle resolved CL has been carried out in the TEM by Yamamoto *et al* [37] using a larger mirror than ours in a 15 mm pole piece gap microscope.

5.0 Conclusions

SEM-CL provided evidence for the opposing effects of carrier distribution volume and surface recombination on grain boundary contrast in CdTe. Monte Carlo simulations indicate that grain boundary contrast in TEM-CL should be greater than SEM-CL, especially for thin specimens where the carrier distribution volume is small due to reduced elastic scattering of the incident electron beam. Measurements on a wedge-shaped CdTe specimen however provided contradictory evidence. The anomaly is attributed to transition radiation. Grain boundary contrast is due to the incoherent luminescence from electron-hole pair recombination and since this is generated from within the foil most of it is lost to total internal reflection and destructive interference. Transition radiation however is generated at the vacuum-specimen interface and is readily collected by the CL ellipsoidal mirrors. The incoherent luminescence is superimposed on a uniform background of coherent transition radiation, thereby reducing grain boundary contrast. The net result is that thicker foils must be used to analyse grain boundaries, which leads to a loss in spatial resolution. Strategies to minimise the effects of transition radiation are also discussed. One method is to exploit the asymmetry in the emission pattern and use only a single CL mirror, located on the side of least transition radiation intensity.

Acknowledgements

K.D. would like to thank EPSRC for funding (EP/J017361/1). Meta data can be accessed via doi:10.15128/5138jd84x.

References

[1] BG Yacobi and DB Holt, *Cathodoluminescence Microscopy of Inorganic Solids*, Plenum Press, New York (1990).
[2] A Losquin, LF Zagonel, V Myroshnychenko, B Rodrííguez-González, M Tencé, L Scarabelli, J Förstner, LM Liz-Marzán, FJG de Abajo and M Kociak, *Nano Lett* **15** (2015) 1229.
[3] V Myroshnychenko, J Nelayah, G Adamo, N Geuquet, J Rodríguez-Fernández, I Pastoriza-Santos, KF MacDonald, L Henrard, LM Liz-Marzán, NI Zheludev, M Kociak and FJG de Abajo, *Nano Lett* **12** (2012) 4172.
[4] BG Mendis, L Bowen and QZ Jiang, *Appl Phys Lett* **97** (2010) 092112.
[5] MJ Romero, H Du, G Teeter, Y Yan and MM Al-Jassim, *Phys Rev B* **84** (2011) 165324.
[6] BG Mendis, MCJ Goodman, JD Major, AA Taylor, K Durose and DP Halliday, *J Appl Phys* **112** (2012) 124508.

[7] F Cléton, B Sieber, A Lefebvre, A Bensaada, RA Masut, JM Bonard, JD Ganière and M Ambri, *J Appl Phys* **80** (1996) 827.
[8] A. Steckenborn, H. Münzel and D. Bimberg, *J. of Luminescence* **24-25** (1981) 351.
[9] M. Merano, S. Sonderegger, A. Crottini, S. Collin, P. Renucci, E. Pelucchi, A. Malko, M. H. Baier, E. Kapon, B. Deveaud and J.-D. Ganière, *Nature* **438** (2005) 479.
[10] BG Mendis, D Gachet, JD Major and K Durose, *Phys Rev Lett* **115** (2015) 218701.
[11] OL Krivanek, JP Ursin, NJ Bacon, GJ Corbin, N Dellby, P Hrncirik, MF Murfitt, CS Own and ZS Szilagyi, *Phil Trans R Soc A* **367** (2009) 3683.
[12] OL Krivanek, TC Lovejoy, N Delby, T Aoki, RW Carpenter, P Rez, E Soignard, J Zhu, PE Batson, MJ Lagos, RF Egerton and PA Crozier, *Nature* **514** (2014) 209.
[13] RH Ritchie and HB Eldridge, *Phys Rev* **126** (1962) 1935.
[14] E Kröger, *Z Physik* **235** (1970) 403.
[15] MJ Hÿtch and WM Stobbs, *Ultramicroscopy* **53** (2004) 191.
[16] M Stöger-Pollach, H Franco, P Schattschneider, S Lazar, B Schaffer, W Grogger and HW Zandbergen, *Micron* **37** (2006) 396.
[17] M Stöger-Pollach, *Micron* **39** (2008) 1092.
[18] AL Frank, ET Arakawa and RD Birkhoff, *Phys Rev* **126** (1962) 1947.
[19] N Yamamoto, A Toda and K Araya, *J Electron Microsc* **45** (1996) 64.
[20] N Yamamoto, H Sugiyama and A Toda, *Proc R Soc Lond A* **452** (1996) 2279.
[21] M Kuttge, EJR Vesseur, AF Koenderink, HJ Lezec, HA Atwater, FJ García de Abajo and A Polman, *Phys Rev B* **79** (2009) 113405.
[22] AA Taylor, JD Major, G Kartopu, D Lamb, J Duenow, RG Dhere, X Maeder, SJC Irvine, K Durose and BG Mendis, *Solar Energy Mat. Solar Cells* **141**, 341 (2015).
[23] IP Jones, *Chemical Microanalysis using Electron Beams*, Institute of Materials (1992).
[24] SJ Pennycook and DE Jesson, *Ultramicroscopy* **37** (1991) 14.
[25] DC Joy, *Monte Carlo Modelling For Electron Microscopy and Microanalysis*, Oxford University Press (1995).
[26] CA Klein, *J Appl Phys* **39**, 2029 (1968).
[27] CM Wolfe, N Holonyak, GE Stillman, *Physical Properties of Semiconductors*, Prentice-Hall Inc, USA (1989).
[28] DP Halliday, MDG Potter, P Dawson, Proc. 28th IEEE Photovoltaics Specialist Conference, Alaska, pp. 521-524.
[29] M Gloeckler, AL Fahrenbruch, JR Sites (2003) Proc. 3rd World Conference PVSEC, Osaka, Japan, pp.491-494.
[30] DA Wood, KD Rogers, DW Lane, JA Coath, *J Phys: Condens Matter* (2000) **12**, 4433.
[31] T Schmidt, K Lischka and W Zulehner, *Phys Rev B* **45** (1992) 8989.
[32] J Lee, NC Giles, D Rajavel and CJ Summers, *Phys Rev B* **49** (1994) 1668.
[33] MJ Romero, MM Al-Jassim, RG Dhere, FS Hasoon, MA Contreras, TA Gessert and HR Moutinho, *Prog Photovolt: Res Appl* **10** (2002) 445.
[34] K Durose, PR Edwards and DP Halliday, *J Crystal Growth* **197** (1999) 733.
[35] NM Boyall, K Durose and IM Watson, *J Microsc* **209** (2003) 41.
[36] BJM Brenny, T Coenen and A Polman, *J Appl Phys* **115** (2014) 244307.
[37] N Yamamoto, FJ García de Abajo and V Myroshnychenko, *Phys Rev B* **91** (2015) 125144.
[38] E Hecht, *Optics*, 4th Edition, Addison Wesley, San Francisco, USA (2002).

Appendix

This section deals with multiple beam interference of the incoherent luminescence generated within a parallel sided foil. As shown schematically in Figure 9 light of electric field amplitude E is generated at depth l within the foil, at an angle θ to the foil normal, and undergoes a series of reflection and transmission events with coefficients r and t respectively. For simplicity the foil is assumed to be non-absorbing. The aim is to calculate the light intensity escaping the top and bottom foil surfaces respectively. It is easy to show that the phase difference δ between any two adjacent rays outside the foil is given by [38]:

$$\delta = \frac{4\pi}{\lambda} nd\cos\theta \qquad \ldots (5)$$

where λ is the photon wavelength in vacuum and n is the refractive index. Note that δ is independent of l. The ray amplitudes at either the top or bottom surfaces follow a geometric series [38]. The light intensity (I) from both surfaces is therefore:

$$I = \frac{E^2 t^2 (1+r^2)}{\left|1 - r^2 e^{i\delta}\right|^2} \qquad \ldots (6)$$

All the variables in the above equation are functions of θ. E is normalised so that the total light intensity generated over all solid angles is unity. Since incoherent luminescence is isotropic this means that $E^2(4\pi/d\Omega) = 1$, where $d\Omega = 2\pi\sin\theta \cdot d\theta$ is the solid angle between θ and $(\theta + d\theta)$. The total intensity is determined by integrating Eq. (6) for values of θ up to the critical angle for total internal reflection. Figures 10a and 10b show the intensity for transverse electric (TE) and transverse magnetic (TM) polarisation as a function of foil thickness respectively. The results are for light at 820 nm wavelength, i.e. peak emission from 'bulk' CdTe (Fig. 7a). Intensity maxima are observed at 140-150 and 290-300 nm foil thickness. The latter may explain the CL intensity peak at 260 nm in Fig. 5c, although the intensity increase there (~29%) is lower than the theoretical values. The reduced contrast is likely to be due to the transition radiation background. This could also explain why no intensity peak was observed at 140-150 nm, since the incoherent luminescence intensity is weaker for smaller foil thicknesses.

Tables

	CL intensity vs. power parameters		
Grain interiors	***A***	***P*$_0$ (μW)**	***k***
G1	43.7 ± 5.2	4.3 ± 0.2	1.46 ± 0.04
G2	45.2 ± 7.8	4.3 ± 0.2	1.46 ± 0.06
G3	59.7 ± 8.9	4.0 ± 0.1	1.43 ± 0.06
Grain boundaries			

GB1	35.9 ± 5.5	5.5 ± 0.1	1.29 ± 0.05
GB2	20.6 ± 3.7	4.3 ± 0.2	1.45 ± 0.06
GB3	27.0 ± 3.5	3.6 ± 0.3	1.42 ± 0.04

Table 1: Best estimates for the power (P) dependence of the CL intensity, i.e. $A(P\text{-}P_o)^k$ where A, P_o and k are fitting parameters. Values are reported for the grain interiors and grain boundaries labelled in Figure 1a.

S_{gb}/S_{sur}	**Electron beam energy**		
	15 keV	**10 keV**	**5 keV**
0.50	15.0%	19.2%	27.6%
0.25	9.2%	12.4%	20.4%
0.10	5.2%	7.7%	15.5%

Table 2: Monte Carlo simulated CdTe grain boundary contrast values (%) in SEM-CL for different electron beam energies and grain boundary recombination velocities. The grain boundary recombination velocity (S_{gb}) is expressed as a fraction of that for a free surface (S_{sur}).

S_{gb}/S_{sur}	**Foil thickness**		
	50 nm	**150 nm**	**250 nm**
0.50	92.0%	71.0%	53.1%
0.25	91.8%	69.8%	50.6%
0.10	91.7%	69.0%	49.0%

Table 3: Monte Carlo simulated, CdTe grain boundary contrast values (%) in TEM-CL for different foil thicknesses and grain boundary recombination velocities. The grain boundary recombination velocity (S_{gb}) is expressed as a fraction of that for a free surface (S_{sur}). The incident electron beam energy is 80 keV.

Figure Captions

Figure 1: (a) Panchromatic CL image of polycrystalline CdTe acquired at 15 keV and 4.2 nA current. CL intensities are extracted from the box regions for grain interiors labelled ‘G1’, ‘G2’ and ‘G3’, as well as grain boundaries ‘GB1’, ‘GB2’ and ‘GB3’. (b) shows the CL intensity variation within the grain interior ‘G1’ as a function of incident electron beam power, while (c) is the equivalent plot for the grain boundary ‘GB1’. The dashed curve is the line of best fit. Colour online.

Figure 2: (a), (b) and (c) are panchromatic CL images of the same CdTe region acquired at 15, 10 and 5 keV beam energy and a near constant power of 20 µW. CL intensity profiles are extracted across the central grain boundary marked with the arrows in (a). The profiles for all three beam energies are shown superimposed in (d). The grain boundary position is 0 nm and the average ‘plateau’ intensity within grain interiors ‘G1’ and ‘G2’ has been normalised to

100% for direct comparison. ‘G1’ is on the left hand side of the grain boundary profile and vice-versa for ‘G2’. Colour online.

Figure 3: Steady state carrier distribution ‘volumes’ in bulk CdTe for (a) 5 keV beam with no grain boundary, (b) 5 keV beam with grain boundary, (c) 15 keV beam with no grain boundary and (d) 15 keV beam with grain boundary. The grain boundary is at 0 nm and has a recombination velocity of 0.5×10^5 cm/s (i.e. half that of the free surface). In all case the electron beam has 10 μW power and is incident at 0 nm position. Colour online.

Figure 4: Many beam, bright-field TEM image of the FIB wedge sample acquired at 200 kV. The different device layers have been identified. A carbon layer was deposited on the CdTe surface as a conductive coating for FIB and electron/ion-beam deposited platinum was used to protect the surface during FIB milling. The arrow indicates the wedge direction with the specimen thickness increasing from right to left.

Figure 5: Simultaneously acquired (a) HAADF and (b) panchromatic CL images from the FIB wedge sample. Individual layers have been labelled in (a), such that 1: glass, 2: SnO_2:F, 3: ZnO/CdS, 4: CdTe, 5: carbon and 6: Pt. The arrow indicates the wedge direction with the specimen thickness increasing from bottom to top. HAADF and CL intensity profiles, extracted from the box region in (a), are shown superimposed in (c). The CL intensity has been suitably scaled so that it can be directly compared with the HAADF intensity. The vertical arrows and associated numbers represent the approximate local specimen thickness at different positions along the wedge; see text for further details. (d) shows the CL profiles across grain boundaries labelled ‘GB1’ and ‘GB2’ in (b). The profiles were extracted from the box regions. The grain boundary is at 0 nm and the average ‘plateau’ intensity within the neighbouring grain interiors has been normalised to 100% for direct comparison. Colour online.

Figure 6: Steady state carrier distribution ‘volumes’ in CdTe for (a) 50 nm thick foil with no grain boundary, (b) 50 nm thick foil with grain boundary, (c) 250 nm thick foil with no grain boundary and (d) 250 nm thick foil with grain boundary. The grain boundary is at 0 nm and has a recombination velocity of 0.5×10^5 cm/s (i.e. half that of the free surface). In all case the 80 keV electron beam is incident at 0 nm position and has 100 pA current. Colour online.

Figure 7: (a) CL spectrum acquired from ~280 nm thick CdTe. (b) Simulated transition radiation spectrum for CdTe foil thicknesses of 260, 280 and 300 nm. (c) and (d) show the CL intensity as a function of position within the CdTe wedge specimen and were extracted from a spectrum image covering wavelength ranges of 760-850 nm and 400-700 nm respectively. The bright intensity on the left hand side of (c) and (d) is due to the CdS layer (cf. Figs. 4 and 5b). The anomalous intensity for some of the pixels in (c) and (d) is due to light collection artefacts. Colour online.

Figure 8: (a) and (b) show number of transition radiation photons emitted within a 350-850 nm wavelength range and the number of steady state carriers as a function of CdTe specimen thickness respectively. (c) and (d) are polar diagrams for transition radiation emission at 600 and 820 nm wavelength from a 280 nm thick CdTe foil. The vertical arrow represents the

direction of the incident electron beam, while the horizontal dashed line represents the thin-foil specimen. The incident beam energy is 80 keV.

Figure 9: Schematic showing multiple beam interference within a thin-foil of thickness *d*. Light is generated at depth *l* within the specimen at an angle θ to the surface normal. *E* is the electric field amplitude of the generated light, while *r*, *t* are the reflection and transmission coefficients.

Figure 10: Intensity of 820 nm wavelength light escaping a CdTe thin-foil specimen plotted as a function of foil thickness for (a) TE-polarisation and (b) TM-polarisation. The intensity is expressed as a percentage of the total light generated.

Figures

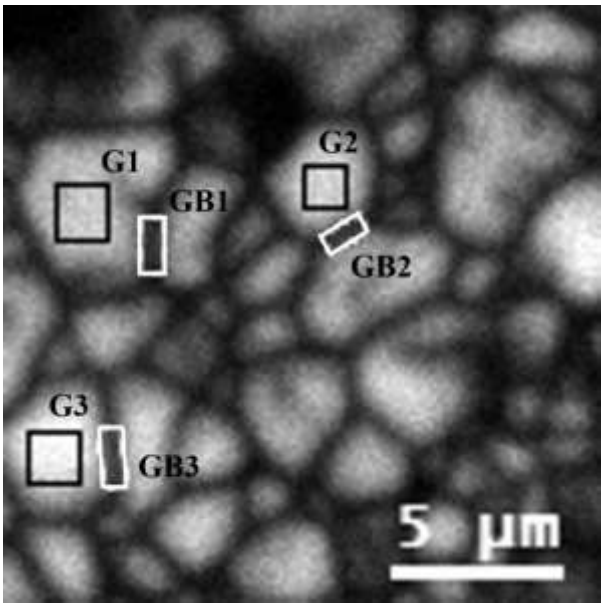

(a)

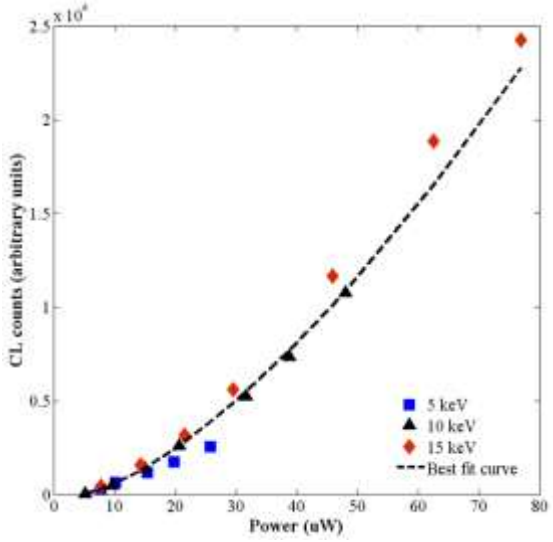

(b)

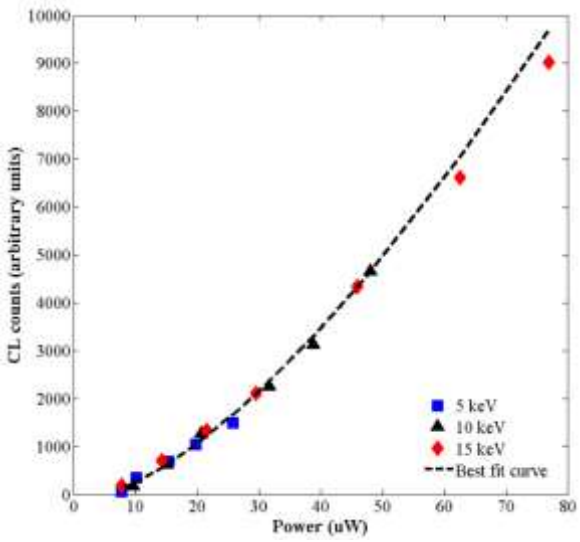

(c)

Figure 1

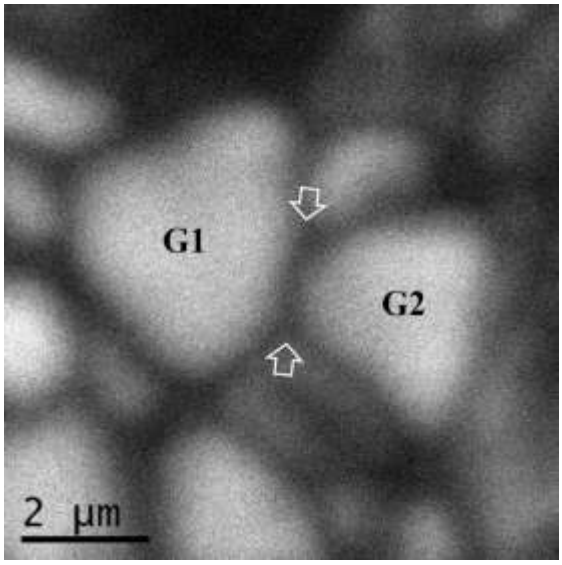

(a)

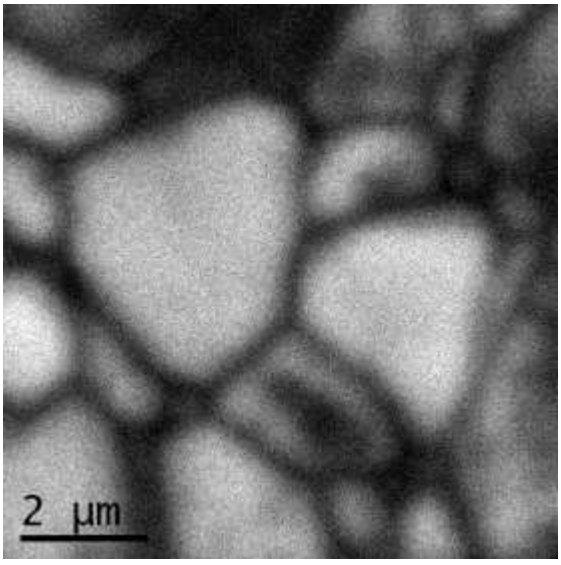

(b)

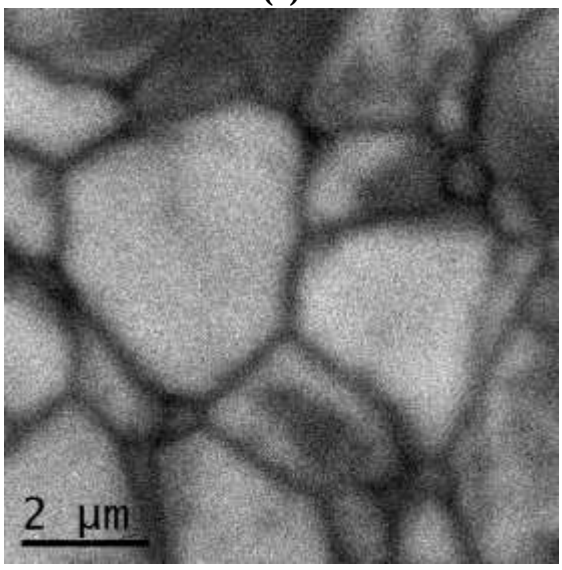

(c)

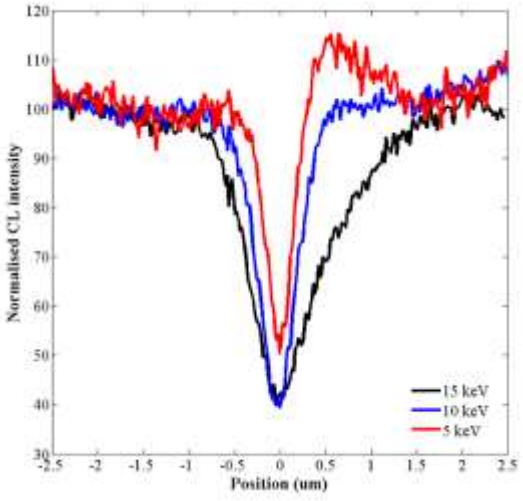

(d)

Figure 2

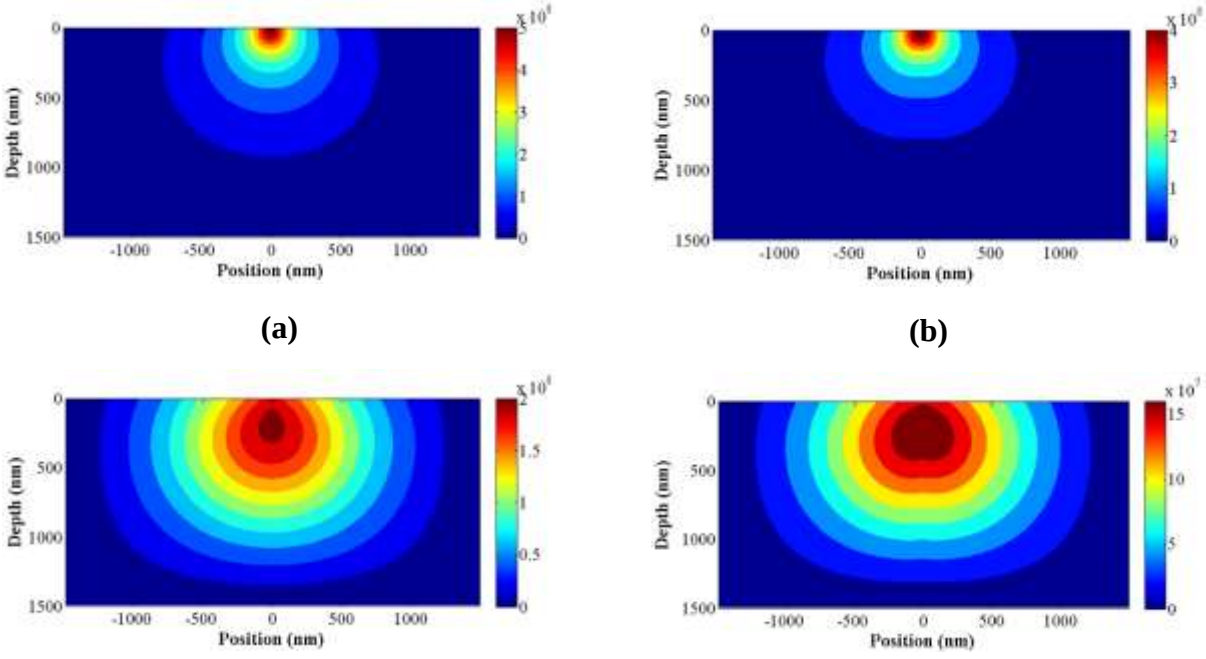

(a) **(b)**

(c) **(d)**

Figure 3

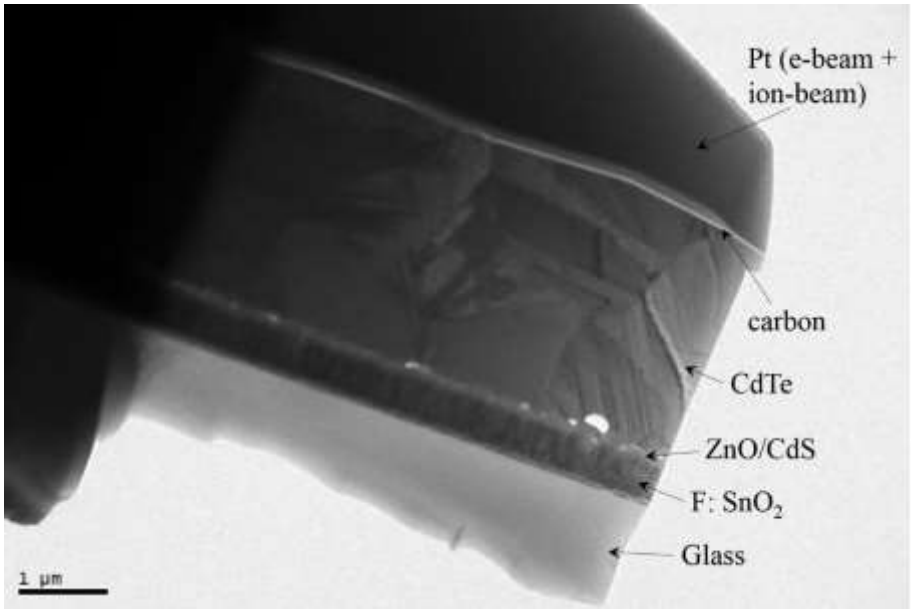
Pt (e-beam + ion-beam)
carbon
CdTe
ZnO/CdS
F: SnO2
Glass
1 µm

Figure 4


1 µm

(a)

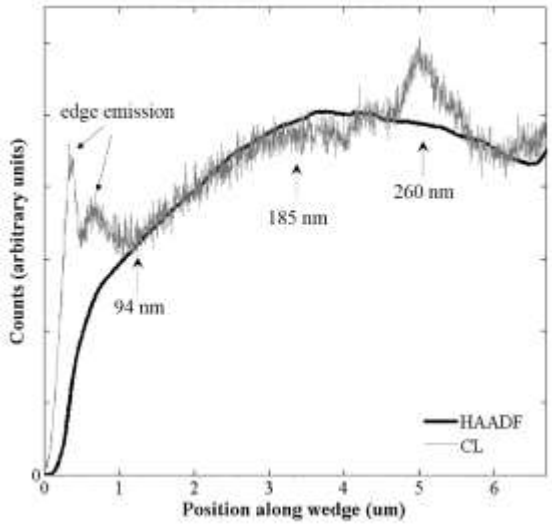
edge emission
94 nm
185 nm
260 nm
HAADF
CL
Counts (arbitrary units)
Position along wedge (um)
0
1
2
3
4
5
6

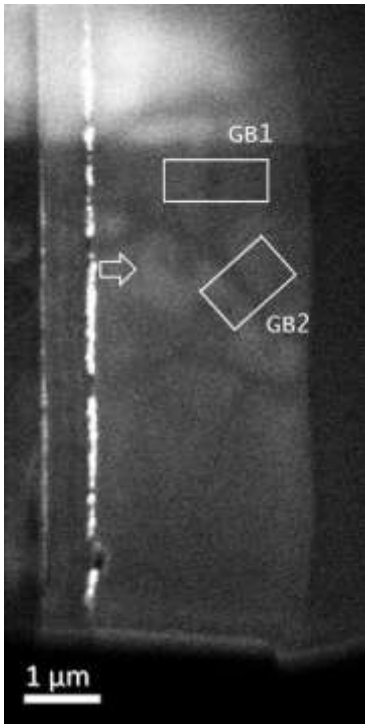

(c)

(b)

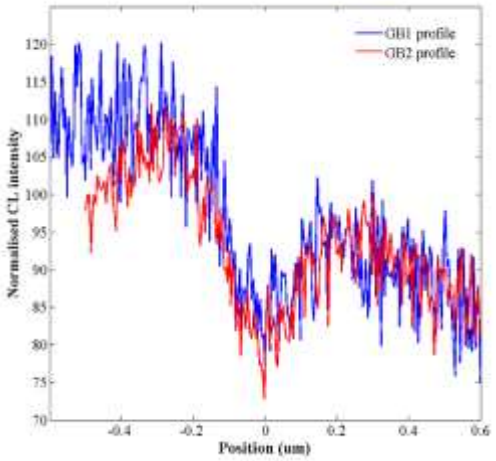

(d)

Figure 5

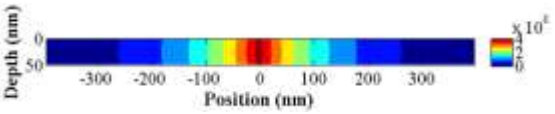

(a)

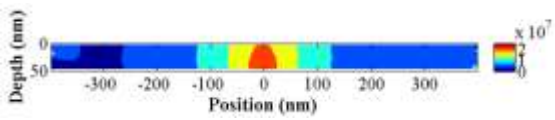

(b)

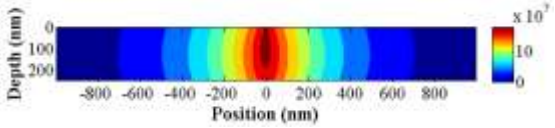

(c)

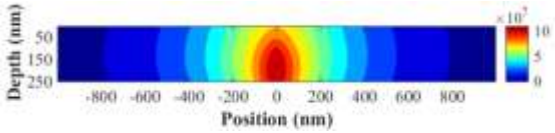

(d)

Figure 6

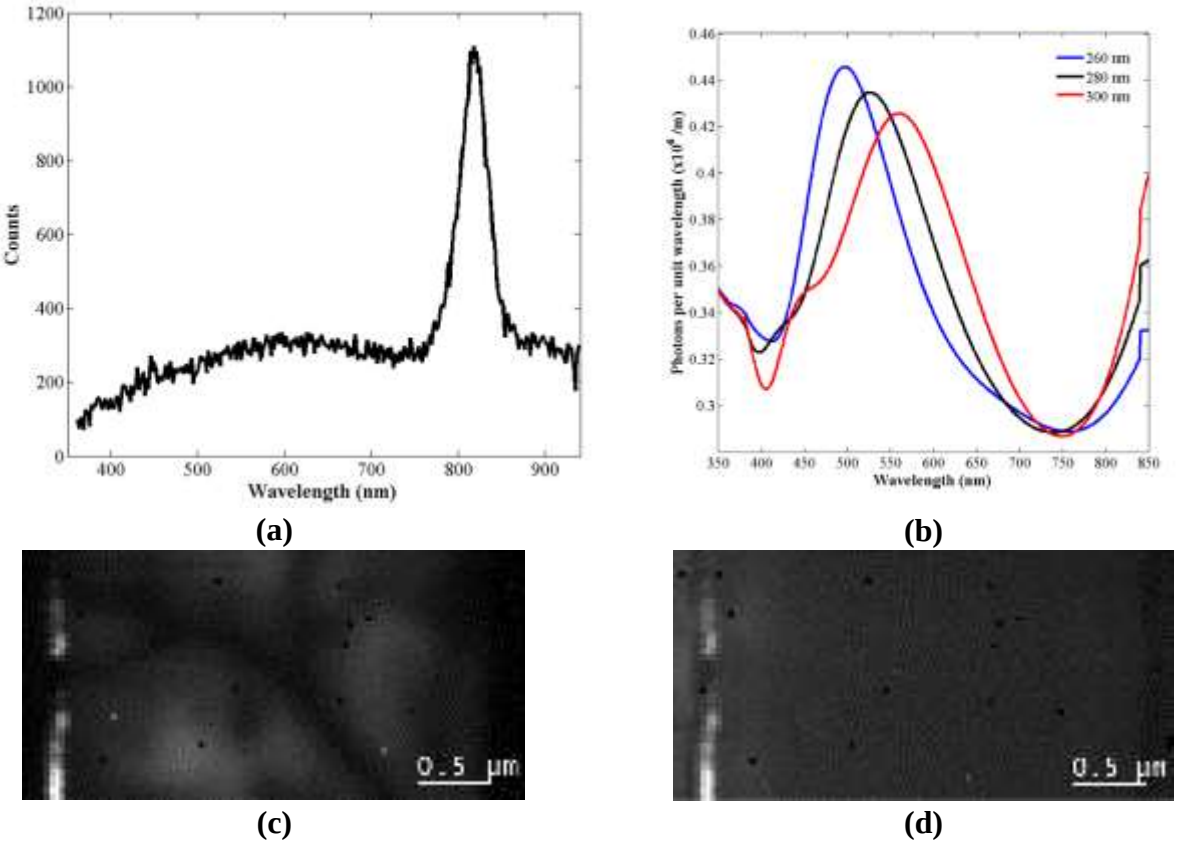

(a) **(b)**

(c) **(d)**

Figure 7

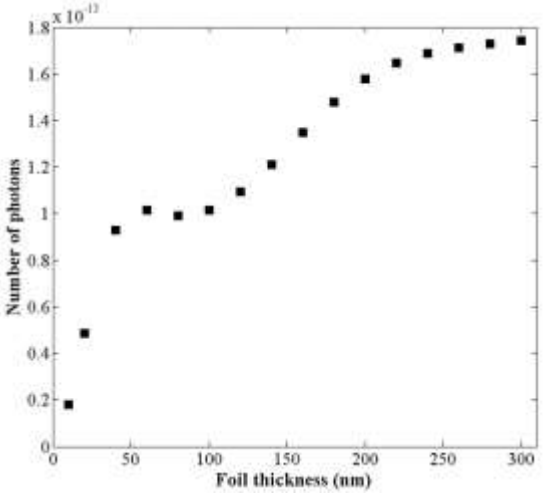
x 10^-13
Number of photons
Foil thickness (nm)

(a)

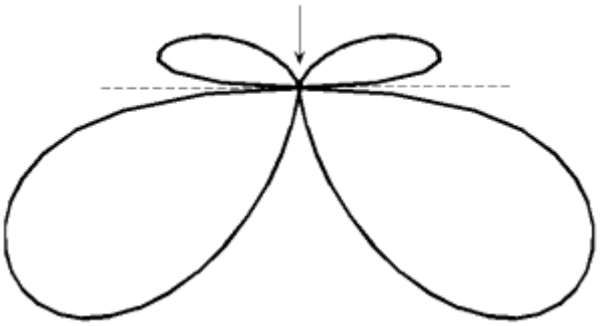

(d)

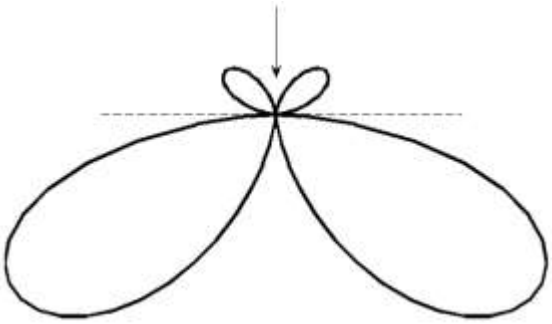

(c)

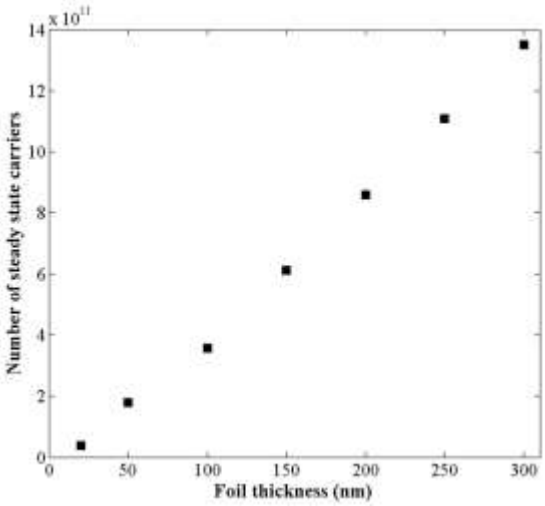
x 10^11
Number of steady state carriers
Foil thickness (nm)

(b)

Figure 8

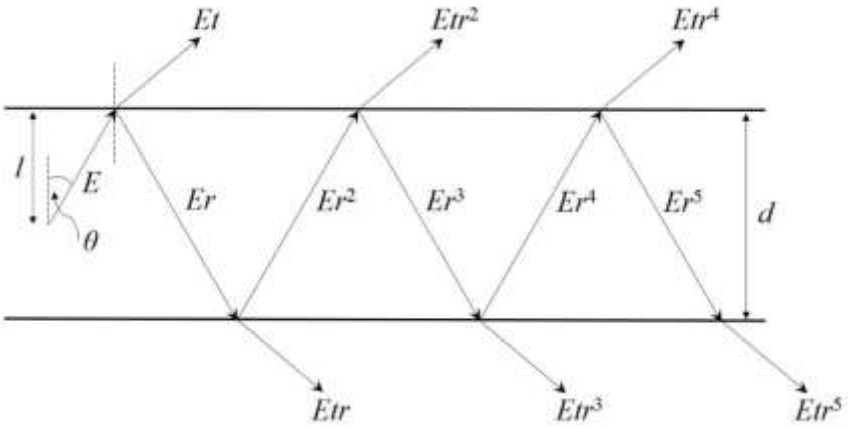

Figure 9

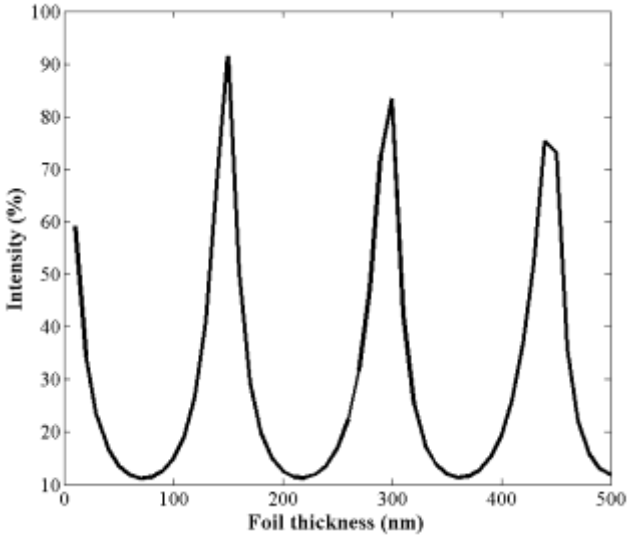

(a)

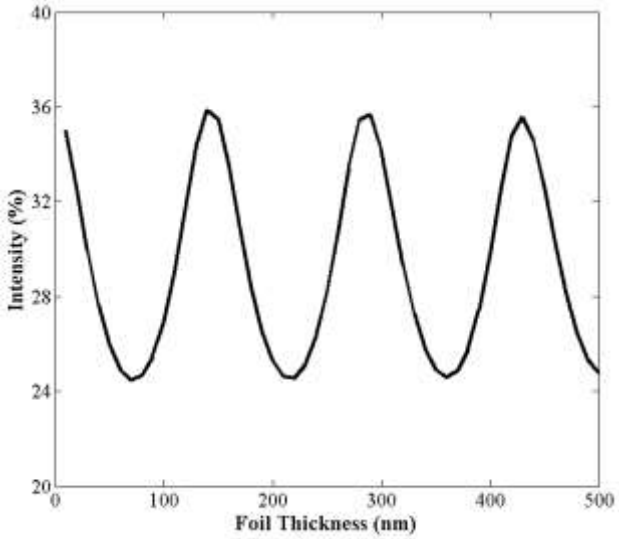
Intensity (%)
Foil Thickness (nm)
40
36
32
28
24
20
0
100
200
300
400
500

(b)

Figure 10